

Dynamical structure factor and a new method to measure the pairing gap in two-dimensional attractive Fermi–Hubbard model

Huaisong Zhao(赵怀松), Feng Yuan(袁峰), Tianxing Ma(马天星), and Peng Zou(邹鹏)
Citation: Chin. Phys. B, 2025, 34 (**11**): 117102. DOI: 10.1088/1674-1056/adfbd9
http://cpb.iphy.ac.cn; http://iopscience.iop.org/cpb

What follows is a list of articles you may be interested in

Ground state of electron-doped *t*-*t*0-*J* model on cylinders: An investigation of finite size and boundary condition effects

Yang Shen(沈阳), Xiangjian Qian(钱湘坚), and Mingpu Qin(秦明普)
Chin. Phys. B, 2025, 34 (**8**): 087105. DOI: 10.1088/1674-1056/add00b

Non-Hermitian birefringent Dirac fermions driven by electromagnetic fields

Kai Liu(刘恺), Wan-Zi Sun(孙万梓), Cheng-Xi Li(李成蹊), and Wu-Ming Liu(刘伍明)
Chin. Phys. B, 2025, 34 (**7**): 077104. DOI: 10.1088/1674-1056/adcaa1

Competing phases and suppression of superconductivity in hole-doped Hubbard model on honeycomb lattice

Hao Zhang(张浩), Shaojun Dong(董少钧), and Lixin He(何力新)
Chin. Phys. B, 2025, 34 (**7**): 077102. DOI: 10.1088/1674-1056/adcb20

Classifying extended, localized and critical states in quasiperiodic lattices via unsupervised learning

Bohan Zheng(郑博涵), Siyu Zhu(朱思宇), Xingping Zhou(周兴平), and Tong Liu(刘通)
Chin. Phys. B, 2025, 34 (**1**): 017103. DOI: 10.1088/1674-1056/ad8cb9

Phase induced localization transition

Tong Liu(刘通), Xingbo Wei(魏兴波), and Youguo Wang(王友国)
Chin. Phys. B, 2024, 33 (**10**): 107103. DOI: 10.1088/1674-1056/ad6a0b

---

RAPID COMMUNICATION

Dynamical structure factor and a new method to measure the pairing gap in two-dimensional attractive Fermi–Hubbard model

Huaisong Zhao(赵怀松)[1], Feng Yuan(袁峰)[1,†], Tianxing Ma(马天星)[2,‡], and Peng Zou(邹鹏)[1,§]

[1] *Centre for Theoretical and Computational Physics, College of Physics, Qingdao University, Qingdao* 266071, *China*
[2] *School of Physics and Astronomy, Beijing Normal University, Beijing* 100875, *China*

(Received 8 August 2025; revised manuscript received 8 August 2025; accepted manuscript online 15 August 2025)

The measurement of the pairing gap is crucial for investigating the physical properties of superconductors or superfluids. We propose a strategy to measure the pairing gap through the dynamical excitations. With the random phase approximation (RPA), we study the dynamical excitations of a two-dimensional attractive Fermi–Hubbard model by calculating its dynamical structure factor. Two distinct collective modes emerge: a Goldstone phonon mode at transferred momentum $\boldsymbol{q} = [0,0]$ and a roton mode at $\boldsymbol{q} = [\pi,\pi]$. The roton mode exhibits a sharp molecular peak in the low-energy regime. Notably, the area under the roton molecular peak scales with the square of the pairing gap, which holds even in three-dimensional and spin–orbit coupled (SOC) optical lattices. This finding suggests an experimental approach to measure the pairing gap in lattice systems by analyzing the dynamical structure factor at $\boldsymbol{q} = [\pi,\pi]$.

Keywords: attractive Fermi–Hubbard model, superfluid, dynamical excitations, roton mode, pairing gap measurement

PACS: 71.10.Fd, 03.75.Kk, 67.85.–d

DOI: 10.1088/1674-1056/adfbd9 **CSTR:** 32038.14.CPB.adfbd9

1. Introduction

The superfluid state of quantum many-body Fermi gases exhibits a nonzero pairing gap (order parameter) originating from the Cooper pairing. Developing a convenient method to measure this pairing gap is essential for understanding many-body pairing phenomena and dynamical excitations. Currently, the pairing gap is primarily obtained by virtue of various excitation processes, such as the momentum-resolved photo-emission spectroscopy[1,2] and the radio-frequency spectroscopy.[3–5] However, these techniques encounter significant challenges in systems with complex band structures.[6–11] Notably, the dynamical excitations offer a powerful alternative for probing the pairing correlations. These excitations are encoded in the dynamical structure factor, which can be experimentally measured through the two-photon Bragg spectroscopy.[12–18]

In continuous Fermi gases, the collective modes are typically probed at a small transferred momentum $\boldsymbol{q}$, whereas the single-particle excitations of the unpaired and paired atoms emerge at a relatively larger $\boldsymbol{q}$. Specifically, the excitations of the paired atoms correspond to the bosonic molecular excitations. In 2008, Vale *et al.* investigated the single-particle excitations at large transfer momenta $q \gg k_{\mathrm{F}}$. They observed that the molecular scattering peak gains increasing spectral weights as the interaction is tuned from the Bardeen–Cooper–Schrieffer (BCS) regime to Bose–Einstein–Condensate (BEC) regime, a behavior distinct from the atomic scattering.[12] Later, they investigated the Goldstone phonon mode and pair-breaking excitation at small $\boldsymbol{q}$, revealing an interaction-induced suppression of the sound speed.[13] Subsequent work demonstrated that the bosonic molecular excitations are sensitive to variations in the pairing gap.[14] Biss *et al.* experimentally characterized the phonon dispersion across the BCS–BEC crossover using the Bragg spectroscopy.[15] Theoretical studies have extensively explored the dynamical structure factors of three-dimensional (3D) Fermi gases.[19–27] For two-dimensional (2D) superfluid Fermi gases, recent experiments using the two-photon Bragg spectroscopy measured the dynamical structure factor across the entire interaction strengths.[28] Notably, Vitali *et al.* used the exact quantum Monte Carlo (QMC) method to investigate the spectral weight redistribution between the molecular and atomic excitations.[29] Several theoretical works on other low-dimensional Fermi gases have investigated the dynamical excitations through the dynamical structure factor.[30,31]

For the discrete ultracold atomic gases, the optical lattice systems generated by superimposing orthogonal standing waves provide an ideal platform for simulating crystalline physics.[32,33] These systems are well described by the

†Corresponding author. E-mail: yuan@qdu.edu.cn
‡Corresponding author. E-mail: txma@bnu.edu.cn
§Corresponding author. E-mail: phy.zoupeng@gmail.com

© 2025 Chinese Physical Society and IOP Publishing Ltd. All rights, including for text and data mining, AI training, and similar technologies, are reserved.

Bose–Hubbard or Fermi–Hubbard models.[34–46] The attractive Fermi–Hubbard model, in particular, has drawn significant theoretical interest due to its relevance to the strongly correlated condensed matter systems.[47–57] Experimentally, this model has been realized in cold atom systems.[58–63] However, to date, no experimental measurement of the dynamical structure factor has been reported for 2D optical lattices. Vitali *et al.* numerically investigated the dynamical structure factor of the half-filled attractive Fermi–Hubbard model on a square optical lattice using the QMC simulations.[64] Their work revealed both the low-energy two collective modes and higher-energy single-particle excitations along the high-symmetry Brillouin zone (BZ) directions. However, the relationship between the roton mode and the pairing gap on an optical lattice remains unclear.

In this paper, we theoretically investigate the doping-dependent dynamical excitations in 2D Fermi superfluids on optical lattices across weak to intermediate coupling regimes. Through detailed analysis of the dynamical structure factor, the key features of both the collective modes and the single-particle excitations are demonstrated, particularly focusing on the roton molecular peak at $\boldsymbol{q}=[\pi,\pi]$. This peak provides a novel strategy for measuring the pairing gap in doped systems with the breaking of particle–hole symmetry, namely, the square of the pairing gap scales linearly with the area under this peak. Notably, this strategy extends to the SOC Fermi gases on an optical lattice, where the complex band structure makes it difficult to directly measure the pairing gap.[65]

This paper is organized as follows. In Section 2, we use the equations of motion of the Green's functions to solve the 2D Fermi–Hubbard model in mean field approximation, and self-consistently obtain the chemical potential and pairing gap. In Section 3, we introduce how to calculate the dynamical structure factor with random phase approximation (RPA). We display results of dynamical structure factor at half-filling and compare with the QMC results in Section 4. In Section 5, we present results when the system is away from half-filling, and discuss the hopping dependence of the sound speed and the dynamical excitations at a transferred momentum $\boldsymbol{q}=[\pi,\pi]$. We check the doping dependence of dynamical structure factor in Section 6. Finally we give our conclusions and acknowledgment, and provide some calculation details in Appendix A.

2. Model and Hamiltonian

An attractive Fermi–Hubbard model in 2D square optical lattices can be described by a Hamiltonian in spatial representation as follows:

$$\begin{aligned} H &= -t\sum_{\langle ij\rangle} C^{\dagger}_{i\sigma}C_{j\sigma} - \mu\sum_{i} C^{\dagger}_{i\sigma}C_{i\sigma} \\ &\quad -U\sum_{i} C^{\dagger}_{i\uparrow}C^{\dagger}_{i\downarrow}C_{i\downarrow}C_{i\uparrow}, \end{aligned} \tag{1}$$

where $\langle ij\rangle$ means the nearest-neighbor sites on the lattice. $C^{\dagger}_{i\sigma}$ ($C_{i\sigma}$) is the creation (annihilation) operator of a particle with spin σ, hopping energy t and chemical potential μ at site i. The Hubbard energy $U>0$ is the strength of the on-site two-body attractive interaction. In the following discussions, U is set to be the unit energy, while the lattice length a_0 is used as unit length. Within the mean field theory, the four-operator interaction Hamiltonian can be dealt into a two-operator one with the definition of pairing gap $\Delta = U\langle C_{i\downarrow}C_{i\uparrow}\rangle$. The pairing gap Δ can be chosen to be a real number in the ground state. Then the above Hamiltonian is displayed into a mean-field one, whose expression in momentum space reads

$$\begin{aligned} H_{\mathrm{MF}} &= \sum_{\boldsymbol{k},\sigma}\xi_{\boldsymbol{k}}C^{\dagger}_{\boldsymbol{k}\sigma}C_{\boldsymbol{k}\sigma} \\ &\quad -\sum_{\boldsymbol{k}}(\Delta^{*}C_{\boldsymbol{k}\downarrow}C_{-\boldsymbol{k}\uparrow}+\mathrm{H.c.})+\frac{|\Delta|^2}{U}, \end{aligned} \tag{2}$$

where $\xi_{\boldsymbol{k}}=-Zt\gamma_{\boldsymbol{k}}-\mu$ and $\gamma_{\boldsymbol{k}}=(\cos k_x+\cos k_y)/2$. The nearest lattice number satisfies $Z=4$ for 2D square lattice.

The above mean-field Hamiltonian can be solved by the equations of motion of the Green's functions. Here we define the diagonal Green's function $G(\boldsymbol{k},\tau-\tau')=-\langle T_\tau C_{\boldsymbol{k}\sigma}(\tau)C^{\dagger}_{\boldsymbol{k}\sigma}(\tau')\rangle$ and off-diagonal one $\Gamma^{\dagger}(\boldsymbol{k},\tau-\tau')=-\langle T_\tau C^{\dagger}_{-\boldsymbol{k}\uparrow}(\tau)C^{\dagger}_{\boldsymbol{k}\downarrow}(\tau')\rangle$. The diagonal Green's function is related to the normal particle density and the off-diagonal Green's function is related to the singlet Cooper pairing information. Their expressions in momentum and energy representation are given by

$$G(\boldsymbol{k},\omega)=\frac{1}{2}\left(\frac{1+\xi_{\boldsymbol{k}}/E_{\boldsymbol{k}}}{\omega-E_{\boldsymbol{k}}}+\frac{1-\xi_{\boldsymbol{k}}/E_{\boldsymbol{k}}}{\omega+E_{\boldsymbol{k}}}\right), \tag{3a}$$

$$\Gamma^{\dagger}(\boldsymbol{k},\omega)=\frac{\Delta^{*}}{2E_{\boldsymbol{k}}}\left(\frac{1}{\omega-E_{\boldsymbol{k}}}-\frac{1}{\omega+E_{\boldsymbol{k}}}\right), \tag{3b}$$

where $E_{\boldsymbol{k}}=\sqrt{\xi^2_{\boldsymbol{k}}+|\Delta|^2}$ is the quasiparticle spectrum. The chemical potential μ and pairing gap Δ are determined by self-consistently solving the density equation and pairing gap equation

$$\begin{aligned} n &= \frac{1}{2}\sum_{\boldsymbol{k}}\left(1-\frac{\xi_{\boldsymbol{k}}}{E_{\boldsymbol{k}}}\right)\tanh\left(\frac{E_{\boldsymbol{k}}}{2T}\right), \\ 1 &= \frac{U}{N}\sum_{\boldsymbol{k}}\frac{1}{2E_{\boldsymbol{k}}}\tanh\left(\frac{E_{\boldsymbol{k}}}{2T}\right). \end{aligned} \tag{4}$$

We have set Boltzmann constant $k_{\mathrm{B}}=1$, and will consider a typical low temperature $T/U=0.01$ (close to zero) in the following analysis.

Generally, the pairing gap Δ exhibits an inverse dependence on the hopping strength t. We plot Δ as a function of t for different particle densities n in Fig. 1. When t is large, Δ asymptotically approaches zero, indicating a phase transition from a superfluid to a normal state. Furthermore, Δ is significantly suppressed as n decreases. It should be noted

that Δ under the mean-field theory is overestimated compared with the corresponding QMC results.[64] For example, at half-filling ($n = 1.0$) with $t/U = 0.25$, the mean-field theory yields $\Delta/U = 0.345$ while the QMC predicts $\Delta/U = 0.1825$. Experimentally, the formation and spatial ordering of nonlocal fermion pairs in an attractive Fermi–Hubbard system are directly observed using two-species degenerate ^{40}K atomic gases.[63]

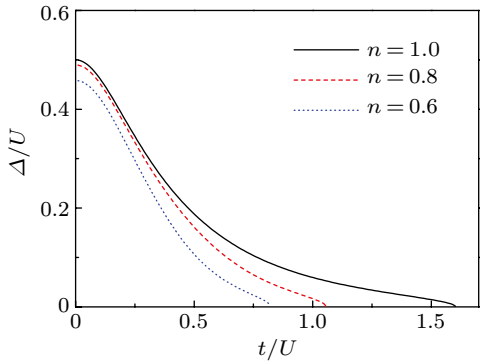


Fig. 1. Pairing gap Δ as a function of t for $n = 1.0$ (black solid line), $n = 0.8$ (red dashed line) and $n = 0.6$ (blue dotted line).

3. Dynamical structure factor and random phase approximation

In this section, we introduce the main idea of the random phase approximation (RPA). The RPA provides an approach to systematically investigate the dynamical excitations by incorporating quantum fluctuations beyond the mean-field theory.

In a superfluid system, there are four different densities, with the normal spin-up/spin-down $\hat{n}_1 = \langle C^\dagger_{i\uparrow} C_{i\uparrow}\rangle$, $\hat{n}_2 = \langle C^\dagger_{i\downarrow} C_{i\downarrow}\rangle$, and the two anomalous densities describing Cooper pairing $\hat{n}_3 = \langle C_{i\downarrow} C_{i\uparrow}\rangle$, $\hat{n}_4 = \langle C^\dagger_{i\uparrow} C^\dagger_{i\downarrow}\rangle$. These four densities are coupled with each other through the finite interaction, where any perturbation in one density induces the correlated fluctuations in other densities. Within the linear response theory, the small external perturbation potential $V_{\rm ext}$ and density fluctuations δn are connected with each other through the full response function χ, namely, $\delta n = \chi V_{\rm ext}$.

The mean-field theory neglects the contribution from the fluctuation term of interaction Hamiltonian, failing to predict the dynamical excitations in interacting systems. In order to incorporate the quantum fluctuations,[66–68] the RPA has been proven to be a reliable method for calculating χ beyond the mean-field level. In a 3D BCS–BEC crossover Fermi superfluid, the dynamical excitations obtained from RPA theory even quantitatively agree well with the experimental results.[15,21,23] Similarly, the 2D RPA incorporating the density fluctuations can qualitatively reproduce the corresponding QMC data.[30] These results indicate that the RPA approach can provide qualitatively reliable predictions for the dynamical excitations of a 2D lattice Fermi superfluid.

The main idea of the RPA is to treat fluctuation Hamiltonian as part of an effective external potential. This theory establishes the relationship between the full response function χ beyond mean-field level and its mean-field response function χ^0,

$$\chi(\boldsymbol{q}, \mathrm{i}\omega_n) = \frac{\chi^0(\boldsymbol{q}, \mathrm{i}\omega_n)}{\hat{1} + \chi^0(\boldsymbol{q}, \mathrm{i}\omega_n) UG}. \tag{5}$$

Here $G = \sigma_0 \otimes \sigma_x$ is a direct product of unit matrix σ_0 and Pauli matrix σ_x.

The numerical calculation of mean-field response function χ^0 is easy to gain, and its expression is given as

$$\chi^0(\boldsymbol{q}, \mathrm{i}\omega_n) = \begin{bmatrix} \chi^0_{11} & \chi^0_{12} & \chi^0_{13} & \chi^0_{14} \\ \chi^0_{21} & \chi^0_{22} & \chi^0_{23} & \chi^0_{24} \\ \chi^0_{31} & \chi^0_{32} & \chi^0_{33} & \chi^0_{34} \\ \chi^0_{41} & \chi^0_{42} & \chi^0_{43} & \chi^0_{44} \end{bmatrix}. \tag{6}$$

The dimension of χ^0 demonstrates the coupling situation among the four density channels. These 16 matrix elements are obtained through the corresponding density–density correlation functions derived from the previously defined Green's functions. Due to all possible symmetries of the system, only 6 of these matrix elements are independent, i.e., $\chi^0_{11} = \chi^0_{22}$, $\chi^0_{12} = \chi^0_{21} = -\chi^0_{33} = -\chi^0_{44}$, $\chi^0_{31} = \chi^0_{32} = \chi^0_{14} = \chi^0_{24}$, $\chi^0_{41} = \chi^0_{42} = \chi^0_{13} = \chi^0_{23}$. The symmetry of the matrix is closely related to the symmetry of the Green's functions, such as $\Gamma^\dagger(\boldsymbol{k}, \omega) = \Gamma(\boldsymbol{k}, \omega) = \Gamma(\boldsymbol{k}, -\omega)$, which leads to $\chi^0_{12} = \chi^0_{21}$, where $\chi^0_{12} = -\left\langle T_\tau C^\dagger_\uparrow(\boldsymbol{r}, \tau) C_\uparrow(\boldsymbol{r}, \tau) C^\dagger_\downarrow(\boldsymbol{r}', \tau') C_\downarrow(\boldsymbol{r}', \tau')\right\rangle$. Based on Wick's theorem, $\chi^0_{12} = -\Gamma^\dagger(\boldsymbol{r} - \boldsymbol{r}', \tau - \tau')\Gamma(\boldsymbol{r}' - \boldsymbol{r}, \tau' - \tau)$. Their expressions are listed in Appendix A.

The total density response function χ_n is defined by $\chi_n \equiv \chi_{11} + \chi_{12} + \chi_{21} + \chi_{22}$, and its expression is given as

$$\chi_n(\boldsymbol{q}, \mathrm{i}\omega_n) = \frac{2\chi_1}{\chi_2 + U\chi_1}, \tag{7}$$

where

$$\chi_1 = \begin{vmatrix} \chi^0_{11} + \chi^0_{12} & 2\chi^0_{14} U & 2\chi^0_{13} U \\ \chi^0_{14} & 1 + \chi^0_{34} U & -\chi^0_{12} U \\ \chi^0_{13} & -\chi^0_{12} U & 1 + \chi^0_{43} U \end{vmatrix}, \tag{8a}$$

$$\chi_2 = \begin{vmatrix} 1 + \chi^0_{34} U & -\chi^0_{12} U \\ -\chi^0_{12} U & 1 + \chi^0_{43} U \end{vmatrix}. \tag{8b}$$

According to the fluctuation–dissipation theory, the density dynamical structure factor $S(\boldsymbol{q}, \omega)$ is connected to the imaginary part of the density response function χ_n by

$$S(\boldsymbol{q}, \omega) = -\frac{1}{\pi} \mathrm{Im}\chi_n(\boldsymbol{q}, \mathrm{i}\omega_n \to \omega + \mathrm{i}\delta), \tag{9}$$

where $\boldsymbol{q}$ and ω are respectively the transferred momentum and energy. δ is a small positive number in the numerical calculation (usually we set $\delta = 0.003$).

4. Results at half-filling

We first study the dynamical structure factor of 2D attractive Fermi–Hubbard model at half-filling ($n = 1$). By analyzing the density dynamical structure factor $S(\boldsymbol{q}, \omega)$ under different transferred momenta $\boldsymbol{q}$, both the collective excitations and single-particle excitations of Fermi atomic gases can be obtained. We calculate the energy and momentum dependencies of $S(\boldsymbol{q}, \omega)$ and present its spectral weight distribution along the high-symmetry directions in the BZ for varying hopping strengths t/U, as shown in Fig. 2. In the low-energy region, $S(\boldsymbol{q}, \omega)$ displays sharp peaks, signaling the presence of two gapless collective modes. The first mode, emerging from $\boldsymbol{q} = [0,0]$, increases nearly linearly with momentum along both $[0,0] \to [\pi,0]$ and $[0,0] \to [\pi,\pi]$. This behavior is characteristic of a phonon mode originating from the spontaneously $U(1)$ symmetry breaking of pairing gap (or order parameter). The slope of this mode at $\boldsymbol{q} = [0,0]$ defines the sound speed. The second mode is the roton mode appearing near $\boldsymbol{q} = [\pi,\pi]$. Its emergence can be attributed to a global pseudospin $SU(2)$ symmetry breaking.[68,71,72] Owing to the particle–hole symmetry of the Hamiltonian (1) at $n = 1$, the fluctuations of superfluid and charge density wave (CDW) become degenerate, leading to the appearance of the gapless roton mode. As the momentum increases, the phonon mode gradually merges into the single-particle excitations, acquiring a finite expansion width because of the scattering processes with the single-particle excitations. The existence of these two collective modes has been confirmed by the QMC simulations.[64]

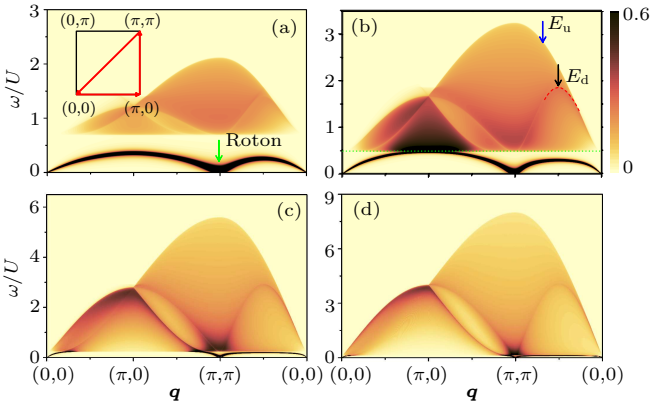


Fig. 2. Color maps of the dynamical structure factor $S(\boldsymbol{q}, \omega)$ as functions of transferred energy and momentum along the high-symmetry directions for hopping strength (a) $t/U = 0.25$, (b) 0.4, (c) 0.7, and (d) 1.0 at half-filling $n = 1$. The red dashed line marks the dispersion of E_d. The green dotted line indicates the minimum energy to break a Cooper pair. Inset in (a): a quarter of the first BZ and three high-symmetry directions (red arrows).

In the high-energy regime, the dynamical excitations are dominated by the single-particle continuum band arising from the pair-breaking effect. The energy required to break Cooper pairs at a certain transferred momentum $\boldsymbol{q}$, given by $E_{\boldsymbol{k}+\boldsymbol{q}} + E_{\boldsymbol{k}}$, is determined by the quasiparticle spectrum $E_{\boldsymbol{k}}$. This pair-breaking process generates a continuous excitation band, with its minimum energy threshold $\min[E_{\boldsymbol{k}+\boldsymbol{q}} + E_{\boldsymbol{k}}]$ marked by a green dotted line in Fig. 2(b). This horizontal green line corresponds to the transferred energy $\omega = 2\Delta$, representing the minimum pair-breaking threshold and providing an experimental strategy for measuring the pairing gap. However, this measurement strategy becomes unreliable in systems with complex band structures (e.g., under SOC), where the threshold varies with $\boldsymbol{q}$. As evident in Fig. 2, increasing t shifts the threshold toward the low energies due to the suppression of the pairing gap. Furthermore, compared with the RPA results, the QMC simulations reveal that the upper single-particle excitation branch has significantly lower energy, highlighting the RPA's limitations in strong interacting systems. To address this, we introduce the quasiparticle coherent weight Z_F[74–77] and a normal-state full Green's function incorporating many-body interaction: $g(\boldsymbol{k}, \omega) = 1/(\omega - \xi_{\boldsymbol{k}} - \Sigma(\boldsymbol{k}, \omega))$, where the self-energy $\Sigma(\boldsymbol{k}, \omega)$ is decoupled as $\Sigma(\boldsymbol{k}, \omega) = \Sigma_e(\boldsymbol{k}, \omega) + \omega\Sigma_o(\boldsymbol{k}, \omega)$. The Z_F is defined as $Z_F^{-1}(\boldsymbol{k}, \omega) = 1 - \Sigma_o(\boldsymbol{k}, \omega)$. Under the static limit approximation, $Z_F = Z_F(\boldsymbol{k} = k_F, \omega = 0)$ by taking the Fermi momentum $\boldsymbol{k} = \boldsymbol{k}_F$, simplifies the full Green's function to $g(\boldsymbol{k}, \omega) = Z_F/(\omega - Z_F\xi_{\boldsymbol{k}}) = Z_F/(\omega - \bar{\xi}_{\boldsymbol{k}})$, where $\bar{\xi}_{\boldsymbol{k}} = Z_F\xi_{\boldsymbol{k}}$ is the renormalized energy spectrum. For the non-interacting systems, $Z_F = 1$. Increasing the interaction strength reduces Z_F, lowering the upper branch energy. In superfluids, Z_F also suppresses the pairing gap, explaining the smaller pairing gap observed in QMC compared with the RPA results. In this paper, we do not discuss the effect of Z_F.

The band width of the single-particle excitations W increases with the hopping term t, specifically, $W = 8t$. Along $[0,0] \to [\pi,\pi]$ direction, $S(\boldsymbol{q}, \omega)$ exhibits a distinct upper boundary, marked by the blue arrow in panel (b), described by

$$E_u = W\sin(\boldsymbol{q}/2) = 8t\sin(\boldsymbol{q}/2). \tag{10}$$

The lower contour, marked by the black arrow in panel (b), is obtained as

$$E_d = 1.83\sin(\boldsymbol{q}). \tag{11}$$

The red-dashed line represents the dispersion of E_d. Physically, E_d does not correspond to a collective mode but is analogous to the 1D lower boundary of $E_d = 4t\sin(\boldsymbol{q})$ at $U = 0$.[69,70] In the Heisenberg model, E_d corresponds to the des Cloizeaux–Pearson (dCP) dispersion.[70] Here, due to the pairing gap, the prefactor is reduced to 1.83, yielding $E_d = 1.83\sin(\boldsymbol{q})$. Notably, $E_d(\boldsymbol{q})$ exhibits double periodicity compared with E_u. Both E_u and E_d arise from the single-particle excitations, which can be understood by $\hbar\omega_{\boldsymbol{kq}} = \xi_{\boldsymbol{k}+\boldsymbol{q}} - \xi_{\boldsymbol{k}}$. Along $[0,0] \to [\pi,\pi]$, this simplifies to $\hbar\omega_{\boldsymbol{kq}} =$

$8t\sin(\boldsymbol{k}+\boldsymbol{q}/2)\sin(\boldsymbol{q}/2)$. When $\sin(\boldsymbol{k}+\boldsymbol{q}/2)=1$, the maximum excitation occurs, yielding $\hbar\omega_{\boldsymbol{kq}}^{\max}=8t\sin(\boldsymbol{q}/2)=E_{\rm u}$. At $n=1$, the Fermi momentum $k_{\rm F}=\pi/2$. When $\boldsymbol{k}=\boldsymbol{k}_{\rm F}$, the excitation energy reduces as $\hbar\omega_{\boldsymbol{kq}}=4t\sin(\boldsymbol{q})=E_{\rm d}$.

5. Results away from half filling

Doping modifies the particle density and shifts the Fermi energy, thereby significantly impacting the dynamical excitations. The particle density is given by $n=1-\delta$, where δ denotes the doping concentration. We analyze the energy and momentum dependencies of $S(\boldsymbol{q},\omega)$ at $n=0.8$ (away from the half-filling). In Fig. 3, we present the contour plots of $S(\boldsymbol{q},\omega)$ along the high-symmetry directions in the BZ for varying hopping strengths. Three key differences emerge when comparing $n=0.8$ with the half-filling, namely, the molecular excitations at $\boldsymbol{q}=[\pi,\pi]$, the split of $E_{\rm d}$, and the doping-dependent variation of the sound speed. These differences are elaborated in the following three subsections.

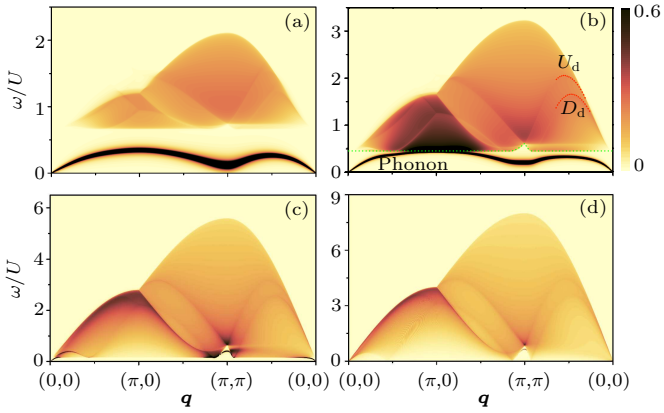


Fig. 3. $S(\boldsymbol{q},\omega)$ along the high-symmetry directions for (a) $t/U=0.25$, (b) 0.4, (c) 0.7, and (d) 1.0 at $n=0.8$. Panel (b) shows $E_{\rm d}$ splitting into $U_{\rm d}$ and $D_{\rm d}$ (blue dotted lines) induced by doping.

5.1. Molecular excitations at $\boldsymbol{q}=[\pi,\pi]$ and its related pairing gap

Compared with Fig. 2, the roton mode minimum at $[\pi,\pi]$ moves above the zero energy when $n=0.8$. Away from the half-filling, the particle–hole symmetry of the system is broken, resulting in opening a gap in this roton mode. In optical lattices, this gapped roton mode remains well separated from the single-particle excitation band and is interpreted as the molecular Cooper-pair excitations here.[71] To show this clearly, Fig. 4 displays $S(\boldsymbol{q},\omega)$ as a function of ω for varying t, with insets highlighting the atomic excitation regime. Obviously, $S(\boldsymbol{q},\omega)$ exhibits two distinct features. First, a sharp low-energy peak corresponds to the excitation of the bosonic molecules from a molecular condensate. Second, a broad high-energy single-particle excitation band arises from the atomic (particle–hole) excitations. As t increases (U decreases), the weight of the molecular peak decreases while the atomic excitation band increases quickly.

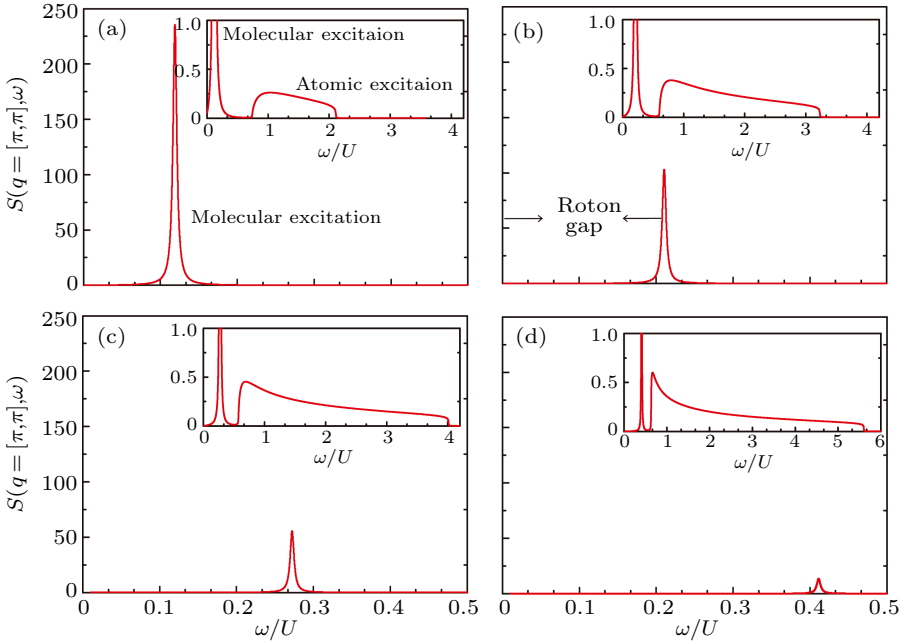


Fig. 4. $S(\boldsymbol{q}=[\pi,\pi],\omega)$ as a function of ω for the hopping strengths (a) $t/U=0.25$, (b) 0.4, (c) 0.5, and (d) 0.7 at $n=0.8$. Insets magnify the atomic excitation regime.

The spectral weight of the molecular peak can be quantified by integrating its intensity over frequency, yielding the peak area $A_{\rm peak}$. In Fig. 5, we plot $A_{\rm peak}$ (pink dotted line) as a function of the hopping strength t, compared with the square of the pairing gap Δ^2 (green solid line). Our results reveal that $A_{\rm peak}$ has almost the same t dependence as Δ^2. Both quantities exhibit particularly large values at small t and decrease gradually as t increases from the intermediate to the weak coupling regime. This correlation indicates that Δ^2 governs the molecular excitation at $\boldsymbol{q}=[\pi,\pi]$, suggesting that Δ can be

experimentally measured by detecting $S(\boldsymbol{q}=[\pi,\pi],\omega)$. It is worth noticing that this measurement method is universal. For 3D cubic optical lattices, our calculations confirm that $A_{\rm peak}$ at the roton mode $\boldsymbol{q}=[\pi,\pi,\pi]$ remains proportional to Δ^2, demonstrating dimensional independence. Furthermore, this method extends to the SOC Fermi systems, where conventional methods for measuring Δ are hindered by the complex band structures.[65]

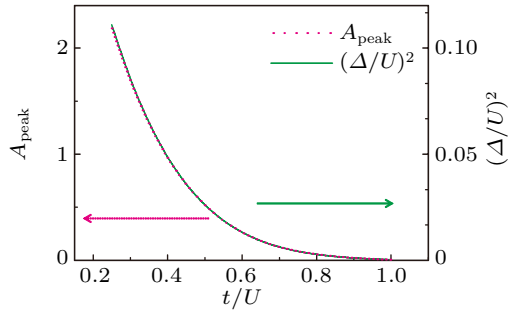


Fig. 5. The area of the molecular peak $A_{\rm peak}$ (pink dotted line) and the square of the pairing gap Δ^2 (green solid line) as a function of t at $n=0.8$.

5.2. The split of $E_{\rm d}$

Doping also significantly modifies the atomic excitations. Compared with the half-filling case in Fig. 2, the boundary $E_{\rm d}$ splits into two distinct branches upon doping. To elucidate this effect, we calculate $S(\boldsymbol{q}=[\pi/2,\pi/2],\omega)$ as a function of ω for varying doping concentrations at $t/U=0.4$ in Fig. 6.

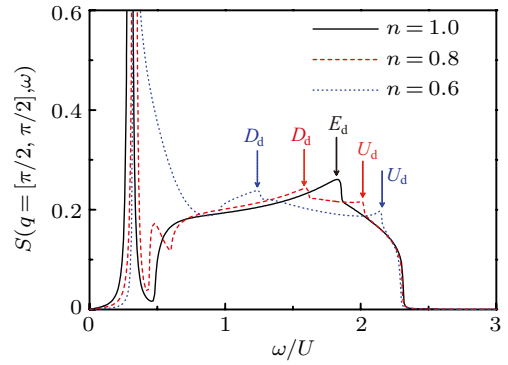


Fig. 6. $S(\boldsymbol{q}=[\pi/2,\pi/2],\omega)$ as a function of ω for $n=1.0$ (black solid line), $n=0.8$ (red dashed line), and $n=0.6$ (blue dotted line) at $t/U=0.4$.

In the low-energy region, a sharp peak emerges as a signature of collective mode excitations, while a broader higher-energy band corresponds to the atomic excitations. At $n=1.0$ (red solid line), a characteristic peak at $\omega/U=1.83$ (marked by a black arrow) corresponds to $E_{\rm d}$. However, for $n=0.8$ (red dashed line) and 0.6 (blue dotted line), $E_{\rm d}$ splits into two branches: $U_{\rm d}$ and $D_{\rm d}$, which also exist in the normal state. This splitting is not induced by the interaction term $H_{\rm int}=-\sum_{\boldsymbol{k}}(\Delta^* C_{\boldsymbol{k}\downarrow}C_{-\boldsymbol{k}\uparrow}+\text{H.c.})$ in Eq. (1). Moreover, as doping increases, the energy gap between $U_{\rm d}$ and $D_{\rm d}$ increases. Along $[0,0]\to[\pi,\pi]$, the Fermi momentum is $k_{\rm F}=\pi/2$ at $n=1.0$ and decreases with doping, thereby altering the single-particle excitation spectrum.

5.3. Hopping dependence of sound speed

The sound speed of the Goldstone phonon mode is defined by its low-energy dispersion in the limit $\omega\to 0$ and $\boldsymbol{q}\to 0$, $c_{\rm s}=\omega/|\boldsymbol{q}|$. The sound speed depends sensitively on the interaction strength, parameterized by t/U. Figure 7 plots $c_{\rm s}$ as a function of t, revealing that $c_{\rm s}$ decreases with decreasing t from the intermediate to the weak coupling regimes. This trend is qualitatively consistent with experimental observation in ^{6}Li Fermi gases.[13,28] The qualitative behavior of $c_{\rm s}$ can be understood through its proportionality to the root-mean-square Fermi velocity $\sqrt{\langle v_{\rm F}^2\rangle}$, which will be introduced in Fig. 9.

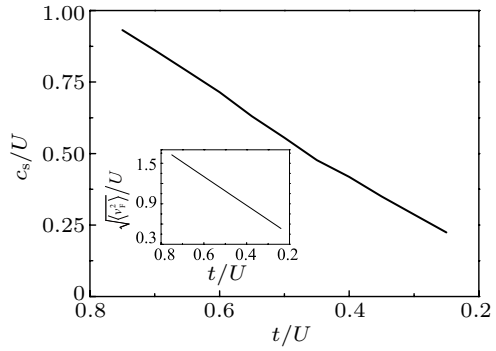


Fig. 7. Sound speed $c_{\rm s}$ as a function of t at $n=0.8$. Inset: $\sqrt{\langle v_{\rm F}^2\rangle}$ versus t.

6. Doping dependence of the dynamical structure factor

Here we discuss the interplay between dynamical excitations and the doping concentration in the Hubbard model. Figure 8 displays $S(\boldsymbol{q},\omega)$ along the high-symmetry directions of the BZ for (a) $n=0.6$ and (b) $n=0.4$ with $t/U=0.4$. Our results reveal two key doping-dependent features: the molecular peak at $\boldsymbol{q}=[\pi,\pi]$ moves to the higher energy, enlarging the roton gap; the sound speed exhibits a pronounced doping dependence. To clarify this, we plot $c_{\rm s}$ as a function of n in Fig. 9(a). Our results show that the sound speed exhibits a non-monotonic doping dependence. It initially increases and then decreases as n increases. This behavior can be qualitatively understood within a weak interaction theory,[73] where $c_{\rm s}$ is closely related to the root-mean-square Fermi velocity, $c_{\rm s}=\sqrt{\langle v_{\rm F}^2\rangle[1-UN(0)]/2}$, with $N(0)$ denoting the density of states (DOS) at the Fermi energy. The DOS is computed as $N(0)=(2\pi)^{-2}\int {\rm d}^2\boldsymbol{k}\delta(\xi_{\boldsymbol{k}})$, and is proportional to the Fermi surface length or n. The Fermi velocity $v_{\rm F}=\partial\xi_{\boldsymbol{k}}/\partial\boldsymbol{k}|_{\boldsymbol{k}=[k_{{\rm F}x},k_{{\rm F}y}]}$ is evaluated at the Fermi wave vector determined by $\xi_{\boldsymbol{k}=[k_{{\rm F}x},k_{{\rm F}y}]}=0$, with $k_{\rm F}$, μ and Δ obtained self-consistently for a given n (see Eq. (4)). We compute the averaged squared Fermi velocity $\langle v_{\rm F}^2\rangle=\frac{1}{N_0}\sum_{\boldsymbol{k}_{\rm F}}v_{\rm F}^2$, where the sum runs over $N_0=120$ points along the Fermi surface. We plot $\sqrt{\langle v_{\rm F}^2\rangle}$ as a function of n in Fig. 9(b). It is shown that $\sqrt{\langle v_{\rm F}^2\rangle}$ has qualitative agreement with the doping

dependence of c_s. At half-filling, v_F exhibits strong anisotropy across the BZ. As n decreases, the Fermi surface contracts, reducing the v_F anisotropy and aligning the system's physical properties with those of continuum Fermi gases. In the low-momentum region, the cosine function can be expanded as $\cos k \approx 1 - k^2/2$, yielding that the energy spectrum of the optical lattice can be approximated as $\xi_{\boldsymbol{k}} \approx Zt(k_x^2 + k_y^2) - tZ - \mu$, which matches the continuum form $\xi_{\boldsymbol{k}} = (k_x^2 + k_y^2)/(2m) - \mu$. Moreover, as $n \to 0$, $N(0) \to 0$, and the sound speed simplifies to $c_s = \sqrt{\langle v_F^2 \rangle}/2$, consistent with ideal continuum Fermi gases.

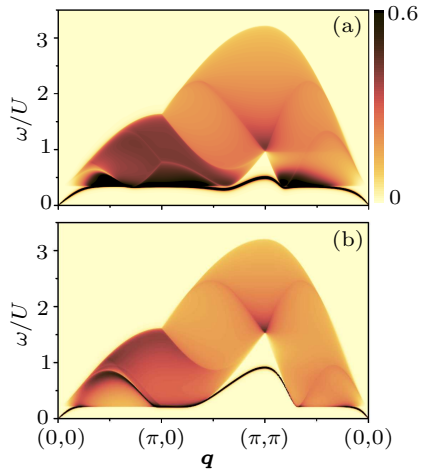


Fig. 8. Color maps of $S(\boldsymbol{q},\omega)$ for (a) $n = 0.6$ and (b) $n = 0.4$ with $t/U = 0.4$.

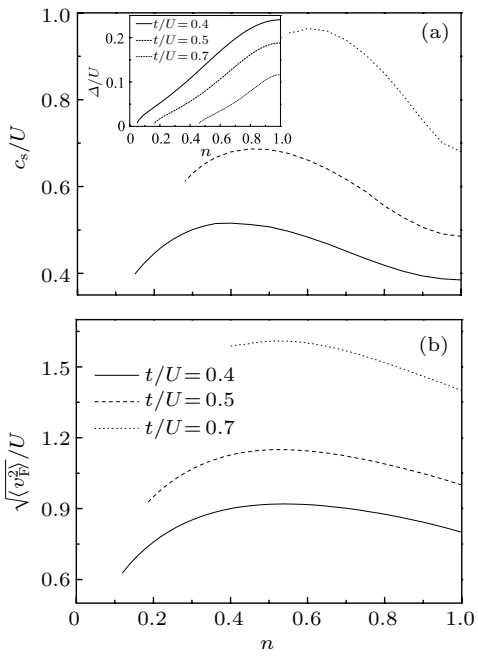


Fig. 9. (a) c_s and (b) $\sqrt{\langle v_F^2 \rangle}$ as functions of n for $t/U = 0.4$ (solid line), 0.5 (dashed line), and 0.7 (dotted line). Inset to (a): the corresponding Δ as a function of n.

7. Summary

In conclusion, the doping and hopping dependencies of the dynamical structure factor in the 2D attractive Fermi–Hubbard model were investigated using RPA theory. Two collective modes emerge: the phonon mode at small transferred momenta and the roton mode at transferred momentum $\boldsymbol{q} = [\pi, \pi]$ regime. The roton mode corresponds to Cooper pair molecular excitations. First, the area of the molecular excitation peak at $\boldsymbol{q} = [\pi, \pi]$ scales with the square of the pairing gap at fixed doping. This observation motivates a universal strategy for measuring the pairing gap, being applicable to both 2D/3D and SOC optical lattices. While this result is obtained from the weak coupling to the intermediate coupling regime within the RPA, we conjecture that it remains valid even for strong interactions. Because this strategy does not depend on dimension and SOC interaction. Furthermore, the relation between the roton mode and the pairing gap is confirmed by both Zhang's theory and Dyke *et al.*'s Bragg experiments. It is also essential to verify this strategy beyond the RPA. Second, the atomic excitation peak splits into two branches when the system deviates from half-filling, with the splitting magnitude increasing with doping. Third, at a given doping, the sound speed is suppressed by interaction strength and governed by the root-mean-square Fermi velocity.

Acknowledgments

This work was supported by the National Natural Science Foundation of China [Grant Nos. U23A2073 (P.Z.) and 11547034 (H.Z.)].

Perceptually uniform color maps ('lajolla') are used in this study.[78]

Appendix A

The mean-field response function χ^0 of 2D interacting Fermi atoms in a square optical lattice is numerically calculated, and all 6 independent matrices elements of χ^0 are

$$\begin{aligned}
\chi^0_{11} &= \frac{1}{4}\sum_{\boldsymbol{k}}\left[1+\frac{\xi_{\boldsymbol{k}}\xi_{\boldsymbol{k}+\boldsymbol{q}}}{E_{\boldsymbol{k}}E_{\boldsymbol{k}+\boldsymbol{q}}}\right]F^{(1)}_{\boldsymbol{k},\boldsymbol{q}} \\
&\quad + \frac{1}{4}\sum_{\boldsymbol{k}}\left[1-\frac{\xi_{\boldsymbol{k}}\xi_{\boldsymbol{k}+\boldsymbol{q}}}{E_{\boldsymbol{k}}E_{\boldsymbol{k}+\boldsymbol{q}}}\right]F^{(2)}_{\boldsymbol{k},\boldsymbol{q}}, \\
\chi^0_{12} &= -\frac{1}{4}\sum_{\boldsymbol{k}}\frac{\Delta^2}{E_{\boldsymbol{k}}E_{\boldsymbol{k}+\boldsymbol{q}}}\left[F^{(1)}_{\boldsymbol{k},\boldsymbol{q}} - F^{(2)}_{\boldsymbol{k},\boldsymbol{q}}\right], \\
\chi^0_{13} &= -\frac{\Delta}{4}\sum_{\boldsymbol{k}}\frac{\xi_{\boldsymbol{k}}+\xi_{\boldsymbol{k}+\boldsymbol{q}}}{2E_{\boldsymbol{k}}E_{\boldsymbol{k}+\boldsymbol{q}}}\left[F^{(1)}_{\boldsymbol{k},\boldsymbol{q}} - F^{(2)}_{\boldsymbol{k},\boldsymbol{q}}\right] \\
&\quad + \frac{\Delta}{4}\sum_{\boldsymbol{k}}\frac{E_{\boldsymbol{k}+\boldsymbol{q}}-E_{\boldsymbol{k}}}{2E_{\boldsymbol{k}}E_{\boldsymbol{k}+\boldsymbol{q}}}F^{(3)}_{\boldsymbol{k},\boldsymbol{q}} \\
&\quad - \frac{\Delta}{4}\sum_{\boldsymbol{k}}\frac{E_{\boldsymbol{k}+\boldsymbol{q}}+E_{\boldsymbol{k}}}{2E_{\boldsymbol{k}}E_{\boldsymbol{k}+\boldsymbol{q}}}F^{(4)}_{\boldsymbol{k},\boldsymbol{q}}, \\
\chi^0_{14} &= -\frac{\Delta}{4}\sum_{\boldsymbol{k}}\frac{\xi_{\boldsymbol{k}}+\xi_{\boldsymbol{k}+\boldsymbol{q}}}{2E_{\boldsymbol{k}}E_{\boldsymbol{k}+\boldsymbol{q}}}\left[F^{(1)}_{\boldsymbol{k},\boldsymbol{q}} - F^{(2)}_{\boldsymbol{k},\boldsymbol{q}}\right] \\
&\quad - \frac{\Delta}{4}\sum_{\boldsymbol{k}}\frac{E_{\boldsymbol{k}+\boldsymbol{q}}-E_{\boldsymbol{k}}}{2E_{\boldsymbol{k}}E_{\boldsymbol{k}+\boldsymbol{q}}}F^{(3)}_{\boldsymbol{k},\boldsymbol{q}}
\end{aligned}$$

$$
\begin{aligned}
&+\frac{\Delta}{4}\sum_{\boldsymbol{k}}\frac{E_{\boldsymbol{k}+\boldsymbol{q}}+E_{\boldsymbol{k}}}{2E_{\boldsymbol{k}}E_{\boldsymbol{k}+\boldsymbol{q}}}F^{(4)}_{\boldsymbol{k},\boldsymbol{q}},\\
\chi^0_{43} &= \frac{1}{4}\sum_{\boldsymbol{k}}\left[1-\frac{\xi_{\boldsymbol{k}}\xi_{\boldsymbol{k}+\boldsymbol{q}}}{E_{\boldsymbol{k}}E_{\boldsymbol{k}+\boldsymbol{q}}}\right]F^{(1)}_{\boldsymbol{k},\boldsymbol{q}}\\
&+\frac{1}{4}\sum_{\boldsymbol{k}}\left[1+\frac{\xi_{\boldsymbol{k}}\xi_{\boldsymbol{k}+\boldsymbol{q}}}{E_{\boldsymbol{k}}E_{\boldsymbol{k}+\boldsymbol{q}}}\right]F^{(2)}_{\boldsymbol{k},\boldsymbol{q}}\\
&+\frac{1}{4}\sum_{\boldsymbol{k}}\left[\frac{\xi_{\boldsymbol{k}}}{E_{\boldsymbol{k}}}-\frac{\xi_{\boldsymbol{k}+\boldsymbol{q}}}{E_{\boldsymbol{k}+\boldsymbol{q}}}\right]F^{(3)}_{\boldsymbol{k},\boldsymbol{q}}\\
&-\frac{1}{4}\sum_{\boldsymbol{k}}\left[\frac{\xi_{\boldsymbol{k}}}{E_{\boldsymbol{k}}}+\frac{\xi_{\boldsymbol{k}+\boldsymbol{q}}}{E_{\boldsymbol{k}+\boldsymbol{q}}}\right]F^{(4)}_{\boldsymbol{k},\boldsymbol{q}},\\
\chi^0_{34} &= \frac{1}{4}\sum_{\boldsymbol{k}}\left[1-\frac{\xi_{\boldsymbol{k}}\xi_{\boldsymbol{k}+\boldsymbol{q}}}{E_{\boldsymbol{k}}E_{\boldsymbol{k}+\boldsymbol{q}}}\right]F^{(1)}_{\boldsymbol{k},\boldsymbol{q}}\\
&+\frac{1}{4}\sum_{\boldsymbol{k}}\left[1+\frac{\xi_{\boldsymbol{k}}\xi_{\boldsymbol{k}+\boldsymbol{q}}}{E_{\boldsymbol{k}}E_{\boldsymbol{k}+\boldsymbol{q}}}\right]F^{(2)}_{\boldsymbol{k},\boldsymbol{q}}\\
&-\frac{1}{4}\sum_{\boldsymbol{k}}\left[\frac{\xi_{\boldsymbol{k}}}{E_{\boldsymbol{k}}}-\frac{\xi_{\boldsymbol{k}+\boldsymbol{q}}}{E_{\boldsymbol{k}+\boldsymbol{q}}}\right]F^{(3)}_{\boldsymbol{k},\boldsymbol{q}}\\
&+\frac{1}{4}\sum_{\boldsymbol{k}}\left[\frac{\xi_{\boldsymbol{k}}}{E_{\boldsymbol{k}}}+\frac{\xi_{\boldsymbol{k}+\boldsymbol{q}}}{E_{\boldsymbol{k}+\boldsymbol{q}}}\right]F^{(4)}_{\boldsymbol{k},\boldsymbol{q}}.
\end{aligned}
$$

The corresponding functions in above equations $F^{(1)}_{\boldsymbol{k},\boldsymbol{q}}$, $F^{(2)}_{\boldsymbol{k},\boldsymbol{q}}$, $F^{(3)}_{\boldsymbol{k},\boldsymbol{q}}$, $F^{(4)}_{\boldsymbol{k},\boldsymbol{q}}$ are defined as

$$
\begin{aligned}
F^{(1)}_{\boldsymbol{k},\boldsymbol{q}} &= A(\boldsymbol{k},\boldsymbol{q},\mathrm{i}\omega_n)-B(\boldsymbol{k},\boldsymbol{q},\mathrm{i}\omega_n),\\
F^{(2)}_{\boldsymbol{k},\boldsymbol{q}} &= C(\boldsymbol{k},\boldsymbol{q},\mathrm{i}\omega_n)-D(\boldsymbol{k},\boldsymbol{q},\mathrm{i}\omega_n),\\
F^{(3)}_{\boldsymbol{k},\boldsymbol{q}} &= A(\boldsymbol{k},\boldsymbol{q},\mathrm{i}\omega_n)+B(\boldsymbol{k},\boldsymbol{q},\mathrm{i}\omega_n),\\
F^{(4)}_{\boldsymbol{k},\boldsymbol{q}} &= C(\boldsymbol{k},\boldsymbol{q},\mathrm{i}\omega_n)+D(\boldsymbol{k},\boldsymbol{q},\mathrm{i}\omega_n),
\end{aligned}
\tag{A1}
$$

where

$$
\begin{aligned}
A(\boldsymbol{k},\boldsymbol{q},\mathrm{i}\omega_n) &= \frac{f(E_{\boldsymbol{k}})-f(E_{\boldsymbol{k}+\boldsymbol{q}})}{\mathrm{i}\omega_n+(E_{\boldsymbol{k}}-E_{\boldsymbol{k}+\boldsymbol{q}})},\\
B(\boldsymbol{k},\boldsymbol{q},\mathrm{i}\omega_n) &= \frac{f(E_{\boldsymbol{k}})-f(E_{\boldsymbol{k}+\boldsymbol{q}})}{\mathrm{i}\omega_n-(E_{\boldsymbol{k}}-E_{\boldsymbol{k}+\boldsymbol{q}})},\\
C(\boldsymbol{k},\boldsymbol{q},\mathrm{i}\omega_n) &= \frac{1-f(E_{\boldsymbol{k}})-f(E_{\boldsymbol{k}+\boldsymbol{q}})}{\mathrm{i}\omega_n-(E_{\boldsymbol{k}}+E_{\boldsymbol{k}+\boldsymbol{q}})},\\
D(\boldsymbol{k},\boldsymbol{q},\mathrm{i}\omega_n) &= \frac{1-f(E_{\boldsymbol{k}})-f(E_{\boldsymbol{k}+\boldsymbol{q}})}{\mathrm{i}\omega_n+(E_{\boldsymbol{k}}+E_{\boldsymbol{k}+\boldsymbol{q}})},
\end{aligned}
\tag{A2}
$$

$f(E_{\boldsymbol{k}})$ and $f(E_{\boldsymbol{k}+\boldsymbol{q}})$ are Fermi distributions.

References

[1] Feld M, Fröhlich B, Vogt E, Koschorreck M and Köhl M 2011 *Nature* **480** 75
[2] Stewart J T, Gaebler J P and Jin D S 2008 *Nature* **454** 744
[3] Fröhlich B, Feld M, Vogt E, Koschorreck M, Zwerger W and Köhl M 2011 *Phys. Rev. Lett.* **106** 105301
[4] Chin C, Bartenstein M, Altmeyer A, Riedl S, Jochim S, Denschlag J H and Grimm R 2004 *Science* **305** 1128
[5] Sommer A T, Cheuk L W, Ku M J H, Bakr W S and Zwierlein M W 2012 *Phys. Rev. Lett.* **108** 045302
[6] Zhai H 2015 *Rep. Prog. Phys.* **78** 026001
[7] Cheuk L W, Sommer A T, Hadzibabic Z, Yefsah T, Bakr W S and Zwierlein M W 2012 *Phys. Rev. Lett.* **109** 095302
[8] Wang P, Yu Z Q, Fu Z, Miao J, Huang L, Chai S, Zhai H and Zhang J 2012 *Phys. Rev. Lett.* **109** 095301
[9] Wang Z Y, Cheng X C, Wang B Z, Zhang J Y, Lu Y H, Yi C R, Niu S, Deng Y, Liu X J, Chen S and Pan J W 2021 *Science* **372** 271
[10] Wu F, Guo G C, Zhang W and Yi W 2013 *Phys. Rev. Lett.* **110** 110401
[11] Han R, Yuan F and Zhao H 2023 *New J. Phys.* **25** 023011
[12] Veeravalli G, Kuhnle E, Dyke P and Vale C J 2008 *Phys. Rev. Lett.* **101** 250403
[13] Hoinka S, Dyke P, Lingham M G, Kinnunen J J, Bruun G M and Vale C J 2017 *Nat. Phys.* **13** 943
[14] Dyke P, Musolino S, Kurkjian H, Ahmed-Braun D J M, Pennings A, Herrera I, Hoinka S, Kokkelmans S J J M F, Colussi V E and Vale C J 2024 *Phys. Rev. Lett.* **132** 223402
[15] Biss H, Sobirey L, Luick N, Bohlen M, Kinnunen J J, Bruun G M, Lompe T and Moritz H 2022 *Phys. Rev. Lett.* **128** 100401
[16] Senaratne R, Cavazos-Cavazos D, Wang S, He F, Chang Y T, Kafle A, Pu H, Guan X W and Hulet R G 2022 *Science* **376** 1305
[17] Li X, Luo X, Wang S, Xie K, Liu X P, Hu H, Chen Y A, Yao X C and Pan J W 2022 *Science* **375** 528
[18] Pagano G, Mancini M, Cappellini G, Lombardi P, Schöfer F, Hu H, Liu X J, Catani J, Sias C, Inguscio M and Fallani L 2014 *Nat. Phys.* **10** 198
[19] Combescot R, Giorgini S and Stringari S 2006 *Europhys. Lett.* **75** 695
[20] Combescot R, Kagan M Y and Stringari S 2006 *Phys. Rev. A* **74** 042717
[21] Zou P, Kuhnle E D, Vale C J and Hu H 2010 *Phys. Rev. A* **82** 061605(R)
[22] Zou P, Dalfovo F, Sharma R, Liu X J and Hu H 2016 *New J. Phys.* **18** 113044
[23] Zou P, Hu H and Liu X J 2018 *Phys. Rev. A* **98** 011602(R)
[24] Hu H, Zou P, and Liu X J 2018 *Phys. Rev. A* **97** 023615
[25] Zou P, Zhao H, He L, Liu X J and Hu H 2021 *Phys. Rev. A* **103** 053310
[26] Kuhnle E D, Hu H, Liu X J, Dyke P, Mark M, Drummond P D, Hannaford P and Vale C J 2010 *Phys. Rev. Lett.* **105** 070402
[27] Watabe S and Nikuni T 2010 *Phys. Rev. A* **82** 033622
[28] Sobirey L, Biss H, Luick N, Bohlen M, Moritz H and Lompe T 2022 *Phys. Rev. Lett.* **129** 083601
[29] Vitali E, Shi H, Qin M and Zhang S 2017 *Phys. Rev. A* **96** 061601(R)
[30] Zhao H, Gao X, Liang W, Zou P and Yuan F 2020 *New J. Phys.* **22** 093012
[31] Gao Z, He L, Zhao H, Peng S G and Zou P 2023 *Phys. Rev. A* **107** 013304
[32] Bloch I, Dalibard J and Zwerger W 2008 *Rev. Mod. Phys.* **80** 885
[33] Wu Z, Zhang L, Sun W, Xu X T, Wang B Z, Ji S C, Deng Y, Chen S, Liu X J and Pan J W 2016 *Science* **354** 83
[34] Greiner M, Mandel O, Esslinger T, Hänsch T W and Bloch I 2002 *Nature* **415** 39
[35] Spielman I B, Phillips W D and Porto J V 2008 *Phys. Rev. Lett.* **100** 120402
[36] Thomas C K, Barter T H, Leung T H, Okano M, Jo G B, Guzman J, Kimchi I, Vishwanath A and Stamper-Kurn D M 2017 *Phys. Rev. Lett.* **119** 100402
[37] Jördens R, Strohmaier N, Günter K, Moritz H and Esslinger T 2008 *Nature* **455** 204
[38] Schneider U, Hackermüller L, Will S, Best T, Bloch I, Costi T A, Helmes R W, Rasch D and Rosch A 2008 *Science* **322** 1520
[39] Greif D, Uehlinger T, Jotzu G, Tarruell L and Esslinger T 2013 *Science* **340** 1307
[40] Hart R A, Duarte P M, Yang T L, Liu X, Paiva T, Khatami E, Scalettar R T, Trivedi N, Huse D A and Hulet R G 2015 *Nature* **519** 211
[41] Parsons M F, Mazurenko A, Chiu C S, Ji G, Greif D and Greiner M 2016 *Science* **353** 1253
[42] Cheuk L W, Nichols M A, Lawrence K R, Okan M, Zhang H, Khatami E, Trivedi N, Paiva T, Rigol M and Zwierlein M W 2016 *Science* **353** 1260
[43] Koepsell J, Bourgund D, Sompet P, Hirthe S, Bohrdt A, Wang Y, Grusdt F, Demler E, Salomon G, Gross C and Bloch I 2021 *Science* **374** 82
[44] Boll M, Hilker T A, Salomon G, Omran A, Nespolo J, Pollet L, Bloch I and Gross C 2016 *Science* **353** 1257
[45] Brown P T, Mitra D, Guardado-Sanchez E, Schauß P, Kondov S S, Khatami E, Paiva T, Trivedi N, Huse D A and Bakr W S 2017 *Science* **357** 1385
[46] Arovas D P, Berg E, Kivelson S A and Raghu S 2022 *Annual Review of Condensed Matter Physics* **13** 239
[47] Scalettar R T, Loh E Y, Gubernatis J E, Moreo A, White S R, Scalapino D J, Sugar R L and Dagotto E 1989 *Phys. Rev. Lett.* **62** 1407
[48] Kyung B, Allen S and Tremblay A M S 2001 *Phys. Rev. B* **64** 075116
[49] Honerkamp C and Hofstetter W 2004 *Phys. Rev. Lett.* **92** 170403
[50] Mondaini R, Nikoliø'c P and Rigol M 2015 *Phys. Rev. A* **92** 013601

[51] Cocchi E, Miller L A, Drewes J H, Koschorreck M, Pertot D, Brennecke F and Köhl M 2016 *Phys. Rev. Lett.* **116** 175301

[52] Strohmaier N, Takasu Y, Günter K, Jördens R, Köhl M, Moritz H and Esslinger T 2007 *Phys. Rev. Lett.* **99** 220601

[53] Ho A F, Cazalilla M A and Giamarchi T 2009 *Phys. Rev. A* **79** 033620

[54] Moreo A and Scalapino D J 2007 *Phys. Rev. Lett.* **98** 216402

[55] Gukelberger J, Lienert S, Kozik E, Pollet L and Troyer M 2016 *Phys. Rev. B* **94** 075157

[56] Paiva T, dos Santos R R, Scalettar R T and Denteneer P J H 2004 *Phys. Rev. B* **69** 184501

[57] Shenoy V B 2008 *Phys. Rev. B* **78** 134503

[58] Mitra D, Brown P T, Guardado-Sanchez E, Kondov S S, Devakul T, Huse D A, Schauß P and Bakr W S 2018 *Nat. Phys.* **14** 173

[59] Brown P T, Guardado-Sanchez E, Spar B M, Huang E W, Devereaux T P and Bakr W S 2020 *Nat. Phys.* **16** 26

[60] Hackermüller L, Schneider U, Moreno-Cardoner M, Kitagawa T, Best T, Will S, Demler E, Altman E, Bloch I and Paredes B 2010 *Science* **327** 1621

[61] Gall M, Chan C F, Wurz N and Köhl M 2020 *Phys. Rev. Lett.* **124** 010403

[62] Schneider U, Hackermüller L, Ronzheimer J P, Will S, Braun S, Best T, Bloch I, Demler E, Mandt S, Rasch D and Rosch A 2012 *Nat. Phys.* **8** 213

[63] Hartke T, Oreg B, Turnbaugh C, Jia N and Zwierlein M 2023 *Science* **381** 82

[64] Vitali E, Kelly P, Lopez A, Bertaina G and Galli D E 2020 *Phys. Rev. A* **102** 053324

[65] Zhao H, Han R, Qin L, Yuan F and Zou P 2024 *Phys. Rev. A* **110** 063326

[66] Liu X J, Hu H, Minguzzi A and Tosi M P 2004 *Phys. Rev. A* **69** 043605

[67] He L 2016 *Ann. Phys.* **373** 470

[68] Ganesh R, Paramekanti A and Burkov A A 2009 *Phys. Rev. A* **80** 043612

[69] Han R, Yuan F and Zhao H 2022 *Europhys. Lett.* **139** 25001

[70] Nocera A, Patel N D, Fernandez-Baca J, Dagotto E and Alvarez G 2016 *Phys. Rev. B* **94** 205145

[71] Zhang S 1990 *Phys. Rev. Lett.* **65** 120

[72] Qin M, Schäfer T, Andergassen S, Corboz P and Gull E 2022 *Annual Review of Condensed Matter Physics* **13** 275

[73] Belkhir L and Randeria M 1994 *Phys. Rev. B* **49** 6829

[74] Schäfer T, Wentzell N, Šimkovic F, He Y Y, Hille C, Klett M, Eckhardt C J, Arzhang B, Harkov V, Le Régent F M, A. Kirsch, Wang Y, Kim A J, Kozik E, Stepanov E A, Kauch A, Andergassen S, Hansmann P, Rohe D, Vilk Y M, LeBlanc J P F, Zhang S, Tremblay A M S, Ferrero M, Parcollet O and Georges A 2021 *Phys. Rev. X* **11** 011058

[75] Hafermann H, van Loon E G C P, Katsnelson M I, Lichtenstein A I and Parcollet O 2014 *Phys. Rev. B* **90** 235105

[76] Feng S, Kuang L and Zhao H 2015 *Physica C* **517** 5

[77] Anderson P W, Lee P A, Randeria M, Rice T M, Trivedi N and Zhang F C 2004 *J. Phys.: Condens. Matter* **16** R755

[78] Crameri F 2018 *Geosci. Model Dev.* **11** 2541